Lee, C. N., Min, K. W., Lee, J.-J., Hwang, J. A., Park, J., Edelstein, J., Han, W. (2011): FUV spectrum in the polar region during slightly disturbed geomagnetic conditions. - Journal of Geophysical Research, 116, A10319

DOI: 10.1029/2011JA016898

FUV spectrum in the polar region during slightly disturbed geomagnetic conditions

C. N. Lee,[1] K. W. Min,[2] J.-J. Lee,[1] J. A. Hwang,[1] J. Park,[3] J. Edelstein,[4] and W. Han[1]

Received 2 June 2011; revised 18 July 2011; accepted 5 August 2011; published 20 October 2011.

[1] We present the results of simultaneous high resolution observations of far ultraviolet (FUV) spectra/images and precipitating electrons made for the polar region during a period of slightly disturbed geomagnetic conditions. The polar region was divided into five subregions: the dayside subauroral region, dayside auroral zone, polar cap, nightside auroral zone, and nightside subauroral region. Precipitation in the dayside subauroral region was dominated by soft electrons, and the intensity of the OI 135.6 nm line relative to the NI 149.3 nm line was significantly enhanced, while electrons of a few keV energies also existed. On the other hand, the nightside subauroral region showed the hardest electron spectrum among the five subregions, and the FUV intensity was the brightest there, with substantial increase in the long Lyman-Birge-Hopfield (LBH) band. The auroral zones showed series of inverted-V events with more energetic electrons in the nightside than in the dayside, and the corresponding FUV auroral features were also brighter and broader in the nightside. In the polar cap region, discrete polar arcs were seen, with corresponding electron beams of ~keV, embedded in the diffuse low-intensity FUV background caused by polar rain. The relative intensity of OI 135.6 nm to the NI 149.3 nm line was evaluated for the five subregions and it was found to decrease with increasing electron characteristic energy when energy was smaller than ~2 keV, and remained more or less the same above ~2 keV, which was confirmed by simulations. On the other hand, the relative intensity of the long LBH band to the short LBH band increased with increasing characteristic energy over the entire energy range up to ~4 keV. The OI 135.6 nm line and long LBH band intensities were compared with the energy flux of precipitating electrons, and they were found to have good correlations. When the energy flux was fitted as a function of the long LBH intensity by a power law, the power index was found to be 1.37 for the entire polar region with ~75 km spatial bins, similar to the value obtained previously for inverted-V events with similar spatial averages.

Citation: Lee, C. N., K. W. Min, J.-J. Lee, J. A. Hwang, J. Park, J. Edelstein, and W. Han (2011), FUV spectrum in the polar region during slightly disturbed geomagnetic conditions, *J. Geophys. Res.*, *116*, A10319, doi:10.1029/2011JA016898.

1. Introduction

[2] An aurora is a visual phenomenon of the upper atmosphere that occurs in the polar region when energetic particles precipitate into the atmosphere and excite the ambient particles, which undergo downward transitions that generally involve forbidden line emissions. Its temporal variations and spatial structures strongly depend on the characteristics of the precipitating particles while the emissions are also related to the conditions of the upper atmosphere and the ionosphere. The precipitating particles originate from solar wind as well as various regions of the magnetosphere, and their characteristics differ according to their source regions. Furthermore, the magnetospheric configuration itself, along with its particle characteristics, changes significantly as it undergoes violent dynamic processes such as magnetic substorms and storms. Hence, there have been continuous efforts to connect the auroral activities to the particle characteristics and to the origins of these particles [*Feldstein and Galperin*, 1985; *Newell and Meng*, 1992, 1995; *Newell et al.*, 1996]. As a result, the polar region is described by its auroral characteristics to consist of the polar cap, where auroras are generally not seen except for occasional sharp arcs, and the auroral zone, where bright structured (discrete) and diffuse auroras are seen, while diffuse auroras can also be seen equatorward of the auroral zone [*Feldstein and Galperin*, 1985]. The polar region can also be classified by the characteristics of the precipitating particles and their connection to the magnetospheric regions,

[1]Korea Astronomy and Space Science Institute, Daejeon, South Korea.
[2]Department of Physics, Korea Advanced Institute of Science and Technology, Daejeon, South Korea.
[3]Helmholtz Centre Potsdam, GFZ Potsdam, Potsdam, Germany.
[4]Space Sciences Lab., University of California, Berkeley, California, USA.

0148-0227/11/2011JA016898

into categories such as polar rain, cusp, central plasma sheet, mantle, low latitude boundary layer, and boundary plasma sheet [*Newell and Meng*, 1992]. Classification based on particle characteristics is sometimes simply made into two zones: the 'hard zone' for particle energies over a few keV and the 'soft zone' for energies typically below 600 eV [e.g., *Hardy et al.*, 1985].

[3] The auroral zone has been observed from numerous space missions using particle instruments as well as imaging cameras: Fast Auroral Snapshot Explorer (FAST), Polar spacecraft, and Image for Magnetopause-to-Aurora Global Exploration (IMAGE). One of the goals of these missions was to establish the relationship between auroral emissions and the characteristics of precipitating particles [*Strickland et al.*, 1983; *Germany et al.*, 1990, 1994]. For example, when a spectrum is observed in space, the intensity ratio of the long wavelength part near 170 nm to the short wavelength part near 140 nm of the LBH band ($a^1\Pi_g - X^1\Sigma_g^+$) is higher for high-energy particles than for less energetic particles, as high-energy particles are able to penetrate more deeply into the atmosphere where the O_2 absorption near 140 nm is significant. Hence, FUV observations with both short and long LBH spectral bands have been used to obtain information on the precipitating auroral particles [*Torr et al.*, 1995; *Paxton et al.*, 1999; *Frey et al.*, 2003]. However, difficulties have been associated with most previous studies, as the observations of the particles and auroral images were carried out on different satellites with different orbital characteristics, and the images themselves were usually taken from high altitudes [*Torr et al.*, 1995; *Brittnacher et al.*, 1997; *Frey et al.*, 2003], providing resolution too poor to resolve detailed auroral features that correspond to the dynamic structures of the precipitating particles [*Kunitake and Oguti*, 1984; *McFadden et al.*, 1987]. In this regard, it should be noted that *Lee et al.* [2010] reported the results of simultaneous observations of both particles and FUV auroral images taken from the same spacecraft that resolved ~km scale structures. They argued that, in the low-resolution images, contributions from backscattered soft secondary atmospheric electrons contaminate the small-scale discrete structures generated by precipitating electrons of higher energies by forming diffuse regions around them.

[4] Ultraviolet (UV) spectroscopic studies have been made for the auroral regions using UV photometers and spectrometers since the early days of space observation [*Joki and Evans*, 1969; *Clark and Metzger*, 1969; *Chubb and Hicks*, 1970; *Gerard and Barth*, 1976; *Huffman et al.*, 1980]. *Paresce et al.* [1983a, 1983b] reported extreme ultraviolet (EUV) spectral characteristics of the dayside and nightside auroras in the wavelength range of 80–140 nm as well as the nightside aurora for the 30–90 nm range with a subnanometer resolution. They identified auroral emission lines from various species such as OI, OII, NI, NII and N_2. *Ishimoto et al.* [1988] measured molecular nitrogen emissions from 110 to 190 nm, covering the whole LBH band, with a 3 nm spectral resolution. Recent observations have generally focused on the global auroral images in selected energy bands rather than on the spectroscopic studies. More recently, however, *Lee et al.* [2010] obtained detailed FUV line spectra in the 134.0–171.5 nm range for inverted-V events with a 0.2–0.3 nm resolution, and showed the dependence of the spectrum according to the energy of the precipitating electrons measured from the same spacecraft.

[5] In this paper, we examine the FUV observations carried out by STSAT-1 for the polar region, which is divided into five subregions: the dayside subauroral region, dayside auroral zone, polar cap, nightside auroral zone, and nightside subauroral region. The FUV spectra, which have peculiar features for each subregion, are compared with characteristic energies of the precipitating electrons for these subregions, and the results are compared with simulations. Finally, the FUV intensities of various emission lines and bands are compared with the energy as well as the energy flux of precipitating electrons.

2. Observations

[6] Our data set was obtained from the observations made on STSAT-1, a dual-purpose mission of astrophysical and geophysical observations, which was launched on 27 September 2003 and operated until May 2005. The satellite was in a 685 km circular sun-synchronous orbit with equatorial crossing at 22:00 LT. The inclination angle was 98.2° and its orbital period was 98.5 min. STSAT-1 is a three-axis stabilized satellite with an accuracy of 5 arcmin attitude control when the star tracker is on for astrophysical observations. For geophysical observations, the accuracy of 5° attitude control was achieved without star tracker corrections. The main scientific payload is an imaging spectrograph, called the Far-ultraviolet Imaging Spectrograph (FIMS), also known as the Spectroscopy of Plasma Evolution from Astrophysical Radiation (SPEAR), capable of measuring FUV emission lines from 90.0 to 115.0 nm (S-band) and 134.0 to 171.5 nm (L-band) with 0.15–0.2 nm and 0.25–0.3 nm spectral resolutions, respectively [*Edelstein et al.*, 2006a, 2006b].

[7] Geophysical observations of FIMS were made only when the geomagnetic conditions were not severe, in order to protect the instrument which was also used for astrophysical purposes. FIMS was directed toward the ground during eclipses for geophysical observations so that it naturally observed auroras and nighttime airglows in the nadir direction. Over the polar region, the plasma instruments aboard the spacecraft, called the Space Physics Package (SPP), measured precipitating electrons simultaneously. The SPP consisted of an Electrostatic Analyzer (ESA), a Solid State Telescope (SST), a Langmuir Probe (LP), and a magnetometer. The ESA, a top-hat type electrostatic analyzer, measured electrons from 100 eV to 20 keV. The SST consisted of two telescopes with their looking directions perpendicular to each other, and measured energetic electrons from 170 keV to 360 keV with silicon detectors while the LP measured ambient thermal electrons. The magnetometer was used to determine the satellite's attitude. For the auroral observations, the satellite was further maneuvered so that the designated one of the satellite's three axes became aligned with the local geomagnetic field line with a 5° accuracy and the ESA could provide pitch angle information of the precipitating electrons. With such a configuration, one of the SST's two telescopes was aligned along the geomagnetic field line while the other was perpendicular to it. More information regarding the instruments and

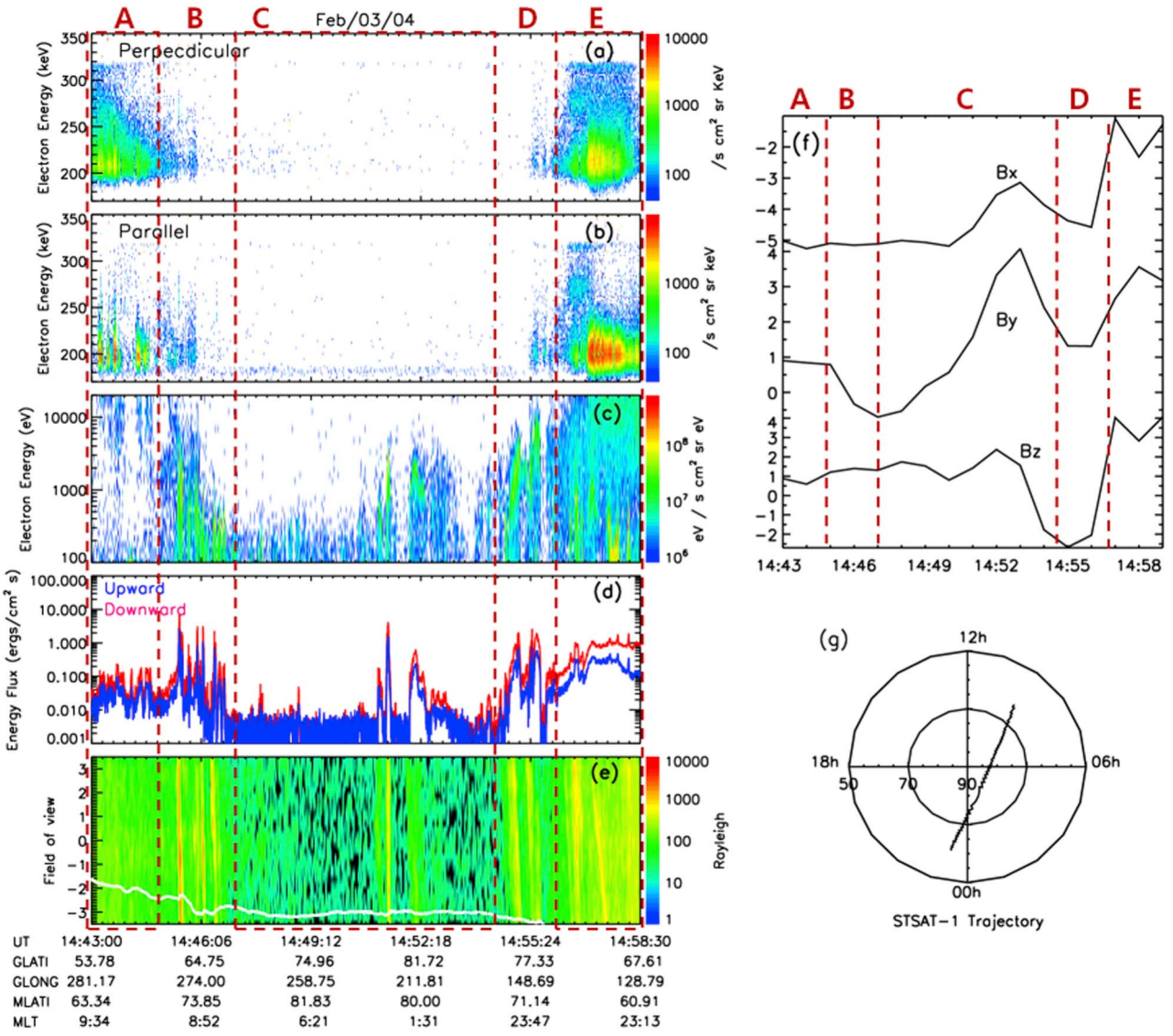

Figure 1. An example of the STSAT-1 observation in the polar region, made on 3 February 2004: (a) the SST energy flux spectrogram in the direction perpendicular to the geomagnetic field line, (b) the SST energy flux spectrogram in the direction parallel to the geomagnetic field line, (c) the ESA energy flux spectrogram for precipitating electrons around a 0° pitch angle, (d) the total energy flux from 100 eV to 20 keV for the electrons moving upward (blue line) and downward (red line) of the geomagnetic field, (e) the FUV image obtained for the wavelength range from 134.0 nm to 171.5 nm, (f) the solar wind magnetic fields estimated at the magnetopause in Geocentric Solar Magnetospheric (GSM) coordinates, and (g) the STSAT-1 trajectory during the time interval of this observation. The white line in Figure 1e of the FIMS image indicates the footprint on the atmosphere of the geomagnetic field line at an altitude of 100 km that passes through the instantaneous satellite location. The magnetic field data were obtained from the OMNI Web site (http://omniweb.gsfc.nasa.gov/).

satellite operations is given by *Lee et al.* [2005] and *Lee et al.* [2010].

3. Results

[8] Auroral observations of STSAT-1 were made from December 2003 to November 2004 as a secondary mission when attitude control of the satellite did not interfere with the operation of the scheduled astrophysical observations. We collected observations of ~200 orbital passes over the pole. The orbital characteristics were favorable for observations of distinct auroral zones with its sun-synchronous orbit: the satellite usually entered the dayside auroral zone from the morning side and crossed the polar cap in the local time sectors of morning to pre-midnight to enter the nightside auroral zone around midnight.

[9] Figure 1 is an example of an observation that includes the distinct polar regions. The observation was made from 14:43:00 to 14:58:30 LT on 3 February 2004, during which the geomagnetic conditions were slightly disturbed

with Dst = −21 nT and Kp = 3+. Figure 1 shows, from the top, the trapped high-energy electrons observed by SST (Figure 1a), the precipitating high-energy electrons observed by SST (Figure 1b), the energy flux spectrogram of precipitating electrons around a 0° pitch angle observed by ESA (Figure 1c), the total energy flux from 100 eV to 20 keV of the electrons moving upward (blue line) and downward (red line) of the geomagnetic field (Figure 1d), the FUV auroral image made by FIMS from 134.0 nm to 171.5 nm (Figure 1e), the solar wind magnetic fields estimated at the magnetopause in Geocentric Solar Magnetospheric (GSM) coordinates (Figure 1f), and the STSAT-1 trajectory during the time interval of this observation (Figure 1g). The field of view (FOV) of the FIMS image in Figure 1e is 7.4°, corresponding to the spatial width of ~76 km at an altitude of 100 km. As Figure 1 shows, the observation had started somewhat before the satellite entered the dayside auroral zone and ended after it had moved out of the nightside auroral zone. Hence, the data set includes part of the outer radiation belts both in the dayside and nightside. The conditions of the interplanetary magnetic field (IMF) varied a little during the course of this observation, as shown in Figure 1f, though the magnitude of the IMF was more or less steady with a value of ~5.2 nT. For example, the Bz component, which had been positive, turned southward right before the satellite entered the nightside auroral zone. Hence, the nightside regions might have been observed during more disturbed conditions than the dayside regions in this particular example.

[10] We have divided the whole observation into five regions according to the particle characteristics based on the SST and ESA measurements: region A, the dayside subauroral region; region B, dayside (or morningside, more accurately) auroral zone; region C, polar cap; region D, nightside auroral zone; and region E, nightside subauroral region. The dayside subauroral region A is characterized by high-energy trapped particles as shown in Figure 1a. Furthermore, in this region, the structured precipitating high energy electrons are seen in Figure 1b, and it is interesting to see that those structures also appear in the ESA channels above several keV. However, they do not produce significant energy flux, as indicated in Figure 1d, and no marked features are noticeable in the FUV image in Figure 1e. The dayside auroral zone B is characterized by structured features (monoenergetic events) of keV electrons, as shown in Figure 1c. The corresponding increase of energy flux is shown in Figure 1d, and the influence of this enhanced keV electron flux is manifested in the FUV auroral image in Figure 1e as discrete features of widths of a few tens of km. In the polar cap region C, most precipitating electrons have very low energy, typically less than a couple of hundred eV, with a low level of flux, as expected from the direct solar wind entry model. Hence, the level of energy flux, as well as the intensity in the FUV image, is the lowest among the five subregions in the present example. However, in this particular example, enhancement of keV electrons is seen in several places in Figure 1c of ESA and in the corresponding energy flux of Figure 1d. The FIMS image in Figure 1e responded well to these events with discrete bright features. The nightside auroral zone D is populated with structured keV electrons, as can be seen in Figure 1c of the ESA energy flux spectrogram and Figure 1d of the total energy flux obtained from ESA. The FIMS image also shows corresponding discrete auroras. In the nightside subauroral region E, enhanced fluxes are seen in both the trapped (Figure 1a) and precipitating (Figure 1b) high-energy electrons of SST. In addition, a high level of structured keV electrons is seen in the ESA observations, embedded in the diffuse spectrum of the high-energy channels above a few keV, as shown in Figure 1c. As a result, the FIMS image in Figure 1e is generally the brightest among the five subregions in the present example, with discrete auroras added on the bright diffuse background, though the footprint of the magnetic field line seems to be a little bit off the field of view of FIMS. In the following sections, we would like to compare the FUV spectra with the energy distribution of the corresponding electron precipitations for each subregion. Since the electrons corresponding to the SST channels do not seem to affect the FUV intensities much, we will focus only on the ESA channels. We start with the dayside and nightside auroral zones, as most of the previous polar region studies focused on these auroral zones.

3.1. Auroral Zones (Regions B and D)

[11] Typical auroral images consist of structured bright arcs embedded in less bright diffuse backgrounds. The dayside auroras are known to appear in the form of multiple fan arcs or rayed bands [*Sandholt et al.*, 2002], and these arcs are generally narrower than those of the nightside region, which is attributed to the fact that the dayside region is more compressed than the stretched nightside tail region [*Feldstein and Galperin*, 1985]. On the other hand, the nightside auroras have complex structures that evolve from rather quiet discrete and curled forms to explosive breakups with the development of substorms. Corresponding electrons generally have softer characteristic energies in the dayside than in the nightside [e.g., *Burch*, 1968]. The example shown in Figure 1 agrees well with these previous observations. Distinguishable discrete auroral features appear in the regions B and D of Figure 1e. The width of the discrete features is ~20–30 km in the dayside (morningside) and more than ~100 km in the nightside. These discrete auroral features correspond well to the spikes in the electron energy flux shown in Figure 1d. It is also interesting to note that the peak energy of the precipitating electrons in the dayside decreases from above several keV to a few hundred eV with increasing magnetic latitude in the poleward direction. A similar trend was observed previously in the late local morning regions [*Frank and Ackerson*, 1971].

[12] Accumulated ESA spectra for the regions B and D are shown in Figure 2 (left). Though they appear to have broad continuous spectra extending to ~10 keV, they actually consist of several inverted-V events with monoenergetic peak energies added on continuous lower energy spectra of a power law shape. For example, the three prominent events of the dayside auroral region seen in Figure 1 have clear peaks in the energy flux spectra, though not shown here. We may note that broadband electron bursts, rather than monoenergetic events, were also previously observed to be the cause of dayside auroral transients [*Newell et al.*, 2010]. It should be noted that the nightside ESA spectrum, shown as a red line, is a bit harder than that of the dayside shown as a

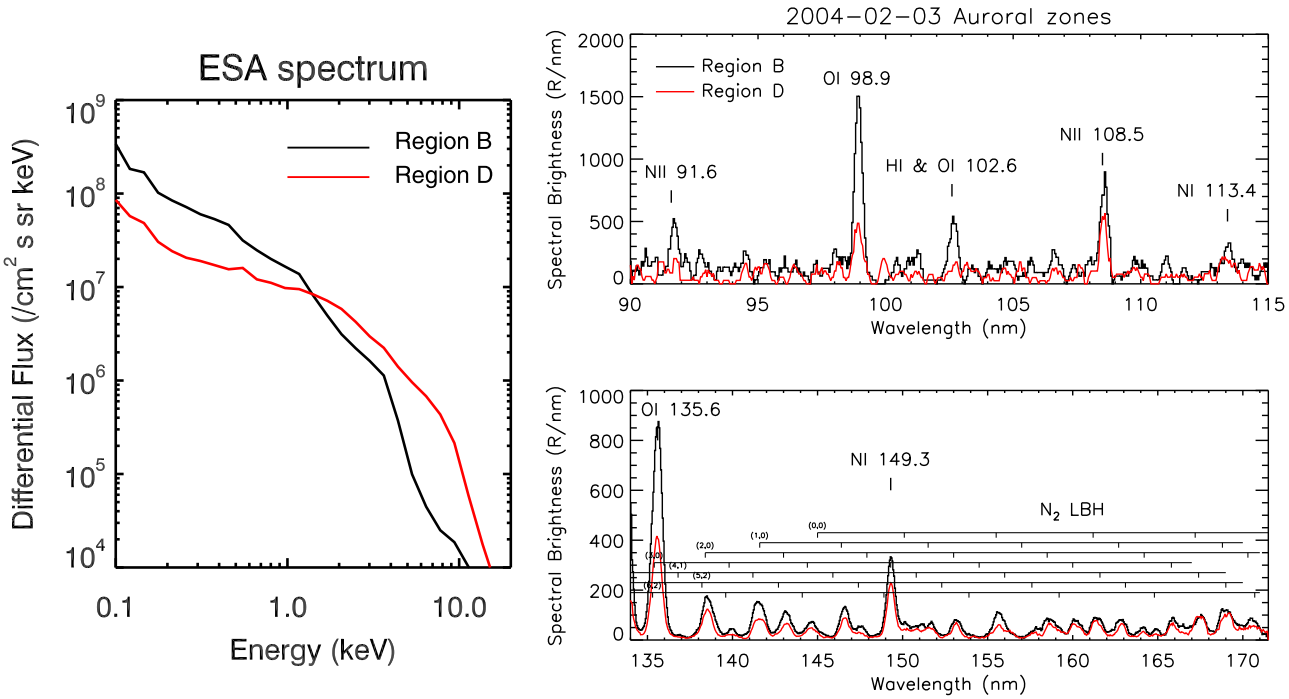

Figure 2. (left) The ESA energy spectra and (right) the corresponding FUV spectra for the auroral zones. (top right) The S-band spectrum and (bottom right) the L-band spectrum. Black solid lines are for the dayside auroral zone from 14:44:50 to 14:47:00 LT and the red solid lines are for the nightside auroral zone from 14:54:30 to 14:56:30 LT of Figure 1.

black line. On the other hand, low energy flux is larger in the dayside than in the nightside in this example.

[13] The corresponding S-band and L-band FUV spectra are shown in Figures 2 (top right) and 2 (bottom right), respectively. In the S-band, the prominent lines are OI 98.9 nm and OI 102.7 nm (not resolved from HI 102.5 nm), along with the ionized nitrogen (NII) line at 108.5 nm. The 91.6 nm NII line is also seen in the dayside spectrum. These NII emission lines are believed to originate from dissociative ionization of N_2 by electron impact [*Victor et al.*, 1976; *Park et al.*, 1977]. In the L-band, the LBH band lines are clearly seen in addition to the dominant OI 135.6 nm and NI 149.3 nm. It is interesting to note that the three OI lines are significantly brighter in the dayside than in the nightside, compared to the relative changes of the NII 108.5 nm and NI 149.3 nm lines as well as the LBH band lines. This could be related to the soft ESA spectrum with high flux at low energies in the dayside. The intensity ratio of the long LBH (LBHL: 160.0–171.5 nm) to the short LBH (LBHS: 140.0–150.0 nm), an indicator of the characteristic energy of precipitating electrons, is ~0.9 in the dayside while it is ~1.2 in the nightside, in agreement with the electron spectrum which is harder in the nightside than in the dayside.

3.2. Subauroral Regions (Regions A and E)

[14] The present example, as depicted in Figure 1, shows diffuse FUV aurora below ~70° MLAT extending to the observation boundaries near ~60° with signatures of trapped high-energy particles. The ESA particle spectra of the dayside subauroral region A and the nightside subauroral region E for the 0° pitch angle are shown in Figure 3 (left), together with the corresponding S-band and L-band FUV line spectra in Figures 3 (top right) and 3 (bottom right), respectively. The ESA measurement for the precipitating electrons in the dayside subauroral region (region A), depicted with a black line, shows a very soft spectrum though the small bump around 5 keV indicates a weak high-energy contribution. On the other hand, the flux levels of the ESA channels are very much enhanced and the spectrum becomes much harder in the nightside subauroral region E as the red solid line shows. The ESA spectrum for the nightside subauroral region E can be fitted with a combination of the two power law distributions with a break near 1 keV, with the power law index ~1.5 for the low energy part and ~0.8 for the high energy part. Figure 1c shows that the low energy part is dominated by the small-scale events while the high energy part is mainly the diffuse precipitation.

[15] The corresponding S-band and L-band FUV spectra are shown in Figures 3 (top right) and 3 (bottom right), respectively. The black solid lines and red solid lines correspond to the dayside and nightside subauroral regions A and E, respectively. As Figures 3 (top right) and 3 (bottom right) show, it is natural to find that the intensities of the S-band and L-band spectra are generally higher in the nightside subauroral region than in the dayside subauroral region since the electron flux level is higher and its spectrum is harder in the nightside than in the dayside, except that the intensity of the OI 98.9 nm line is higher in the dayside subauroral region than in the nightside subsuroral region. In fact, the FIMS intensity levels are the highest in the nightside subauroral region as the ESA flux level is the highest among all the subregions and the spectrum is the hardest, extending beyond 20 keV. For example, the intensity of the NII 108.5 nm line, which is virtually nonexistent in the

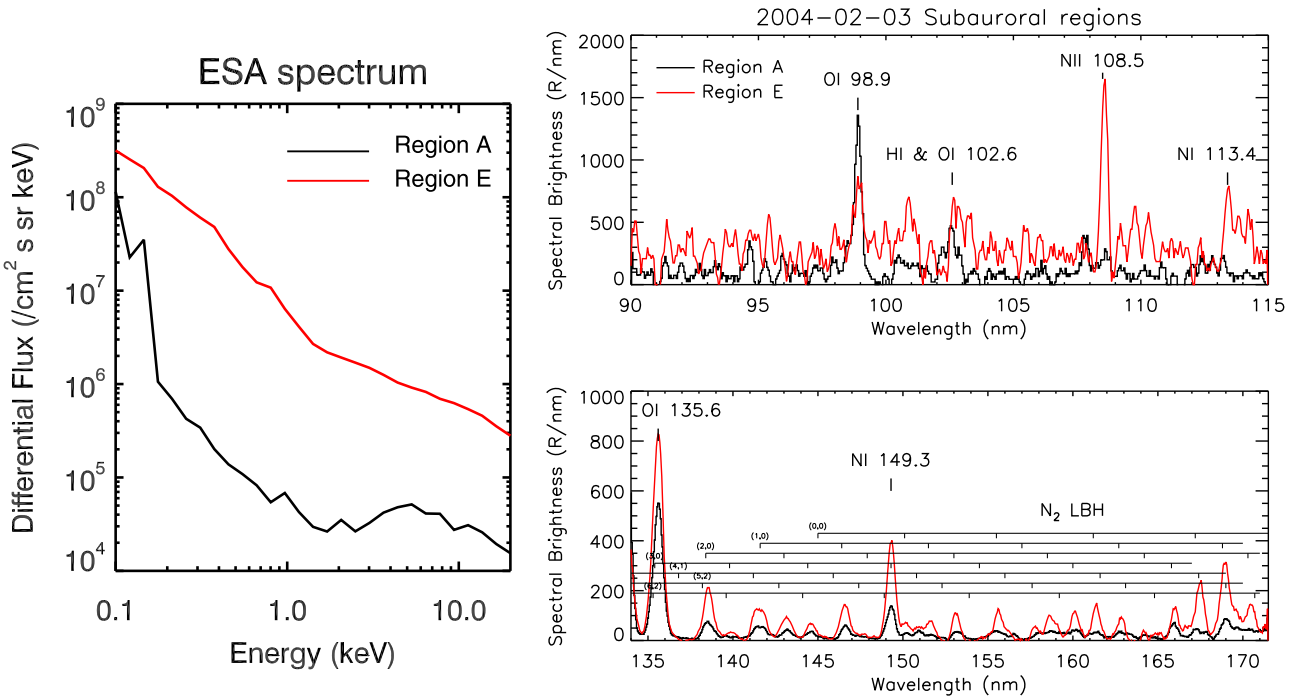

Figure 3. (left) The ESA energy spectra and (right) the corresponding FUV spectra for the subauroral regions. (top right) The S-band spectrum and (bottom right) the L-band spectrum. Black solid lines are for the dayside subauroral region from 14:43:00 to 14:44:50 LT and the red solid lines are for the nightside auroral zone from 14:56:30 to 14:58:30 LT of Figure 1.

dayside subauroral region, is ~50% higher than that of the nightside auroral zone, reflecting the electron flux enhancement at high energies in the nightside subauroral region compared to the nightside auroral zone. On the other hand, the intensity of the NI 149.3 nm line does not increase much from the nightside auroral zone value, probably because of the absorption by O_2. The intensity of the OI 135.6 nm increases over its counterpart in the dayside subauroral region, in accordance with the increase of the electron flux. The intensity of the LBH lines increases from the values in the dayside subauroral region and its enhancement is more significant in the long LBH bands, as the long LBH lines are not affected by the O_2 absorption. The intensity ratio of LBHL to LBHS bands is ~1.5 for the dayside subauroral region and ~1.8 for the nightside subauroral region E. Both of these values are higher than those for the dayside and nightside auroral zones.

3.3. Polar Cap Region (Region C)

[16] In the polar cap region, a weak precipitation of electrons around a few hundred eV is known to exist, which is believed to originate from solar wind [*Winningham and Heikkila*, 1974]. These soft electrons, known as polar rain, do not produce significant auroral emission, leaving a hole in the poleward region of the auroral oval in the global image of the polar region. An example of the polar rain observed by STSAT-1 is seen in Figures 1c and 1d of the ESA measurements in the polar cap region C. The electron energy is generally observed to be lower than a few hundred eV and the flux level is also low. Hence, the level of the precipitating energy flux is lowest among the five subregions and the intensity of the FUV image is also the lowest. However, in the present particular example, a few incidents of enhanced particle precipitation and the corresponding brightening of the FUV emission are observed inside the polar cap region. The bright feature seen from 14:51:20 to 14:51:25 LT has a width of ~70 km. Without a global image, it is not clear whether these bright features are part of the so-called "theta aurora" which spans across the polar cap region and is observed most frequently during the positive Bz [*Frank et al.*, 1982, 1986; *Gussenhoven*, 1982], in association with monoenergetic electron precipitations of several keV [*Frank et al.*, 1985; *Makita et al.*, 1991], though polar arcs do occur under the conditions of the southward IMF [*Sandholt et al.*, 2006]. Nevertheless, the observation of the polar arcs shown in Figure 1 was made with the northward IMF before its southward turning, and the precipitating electrons seem to have monoenergetic features embedded in the low energy background, as shown Figure 1c. We distinguish between these diffuse and discrete FUV emissions in the following discussions.

[17] Figure 4 (left) shows the electron energy spectrum obtained from ESA, and Figure 4 (right) shows the corresponding S- and L-band FUV line spectra. The black lines correspond to the observations made during the time interval from 14:47:00 to 14:51:00 LT, in which only the diffuse emission is seen and the regions of bright discrete emission are excluded. The red lines correspond to the observations made during the time interval from 14:51:20 to 14:52:30 LT, in which the bright discrete emission is the dominant contribution. The observed polar rain electrons, depicted as a black line in the ESA plot, show a very soft spectrum with a sharp decrease with increasing energy. The corresponding S-band FUV spectrum shows the enhancements

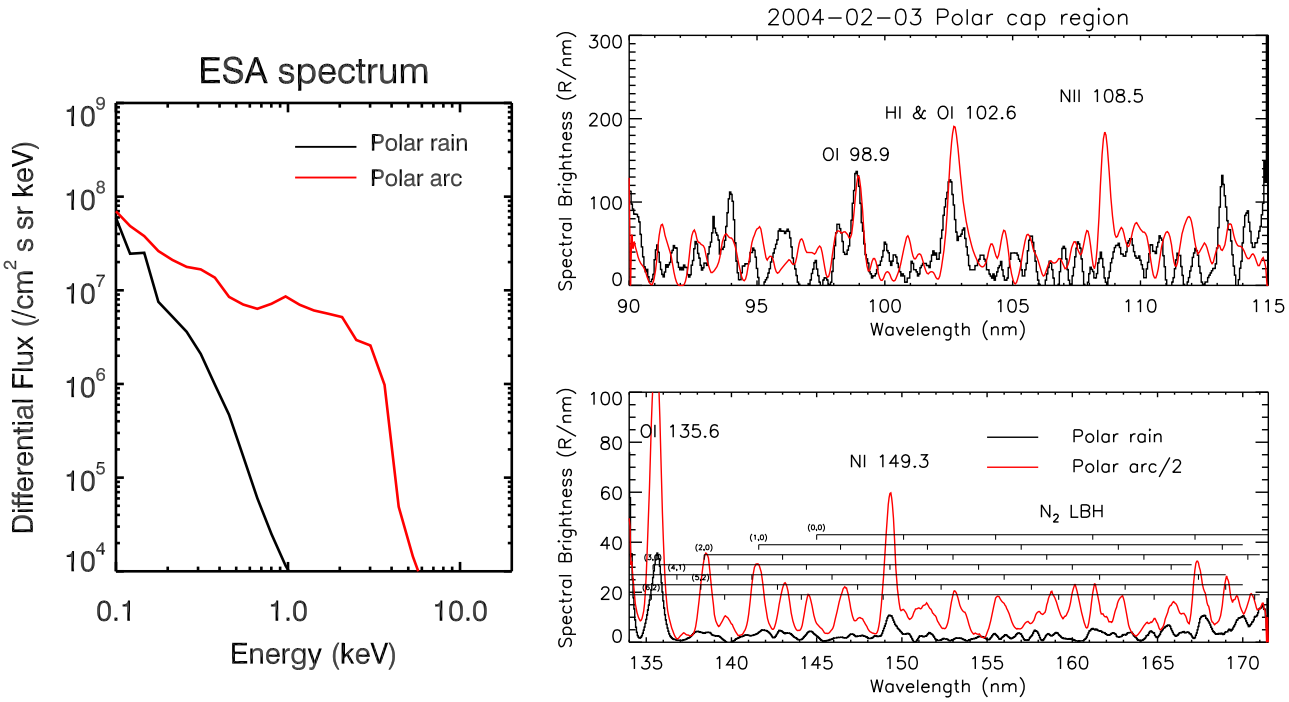

Figure 4. The ESA energy spectra and (right) the corresponding FUV spectra for the subauroral regions. (top right) The S-band spectrum and (bottom right) the L-band spectrum. Black solid lines are for the polar rain region from 14:47:00 to 14:51:00 LT and the red solid lines are for the polar arc region from 14:51:20 to 14:52:30 LT of Figure 1.

at OI 98.9 nm and HI and OI 102.6 nm as well as NI 113.4 nm above the level of fluctuations. It is interesting to note that the 102.6 nm line, an unresolved mixture of OI 102.7 nm and HI 102.5 nm, has an intensity comparable to the OI 98.9 nm line while the intensity of the OI 98.9 nm line is always higher than that of the 102.6 nm line in other subregions. The L-band spectrum shows the OI 135.6 nm line and a bump at 149.3 nm where the NI emission line exists. However, the LBH band lines are not clear though the wavy features may actually correspond to those lines.

[18] On the other hand, the ESA electrons measured during the time interval from 14:51:20 to 14:52:30 LT, corresponding to the bright discrete features, show a hard spectrum with a flat shape up to 4 keV and a sharp cut-off near 4 keV, as indicated by a redline in Figure 4 (left). The spectrum consists of a low energy background, corresponding to polar rain, and the high flux level of monoenergetic electrons. The corresponding FUV spectra are shown as red lines in Figure 4 (right). First, we note in the S-band spectrum that the prominent NII 108.5 nm line, which was nonexistent in the polar rain region, is now seen in the polar arc region, probably because of the energetic particles associated with the polar arcs. The intensity of the OI 102.6 nm line, mixture of the OI 102.7 nm and HI 102.5 nm lines is enhanced and it is interesting to note that the peak of the OI 102.6 nm line seems to shift a little bit toward the longer wavelength compared to that of the polar rain spectrum depicted in black. This shift may have been caused by the enhanced contribution from OI 102.7 nm rather than from HI 102.5 nm with a more energetic particle precipitation in the polar arc region than in the polar rain region. In the L-band, the OI 135.6 nm line as well as the NI 149.3 nm line and LBH bands show significantly increased intensities compared to those of the polar rain.

4. Discussion

[19] We discussed the particle characteristics and the corresponding FUV spectra for five distinct polar regions, based on the data from a single pass. This data set included most of the essential features that occur during slightly disturbed geomagnetic conditions: diffuse and discrete auroras and low intensity emissions in the polar cap, in which polar cap arcs are embedded. The observed FUV spectra corresponded well to their respective particle characteristics. We have examined all the data collected from ~200 satellite orbits, most of which were observed during geomagnetically quiet times. In general, the nightside auroral zone was the brightest in FUV emissions and on rare occasions of slight disturbances, electron precipitation was seen both in the ESA channels and the SST channels, especially in the auroral zone boundaries or below, and the corresponding FUV emission was particularly bright. Hence, the present example can be considered more or less a typical one that occurs during a slightly disturbed time except that the FUV emission is the brightest in the nightside subauroral region in the present case.

[20] *Germany et al.* [1990] reported the results of simulation studies that the intensity ratio of OI 135.6 nm to LBHL (183.8 nm) is more sensitive to the changes in the characteristic energy, showing a change of 13 over the range from 200 eV to 10 keV, than that of LBHS (146.4 nm) to LBHL, which is about a factor of 3. The difference is especially significant at low energies. For example, the

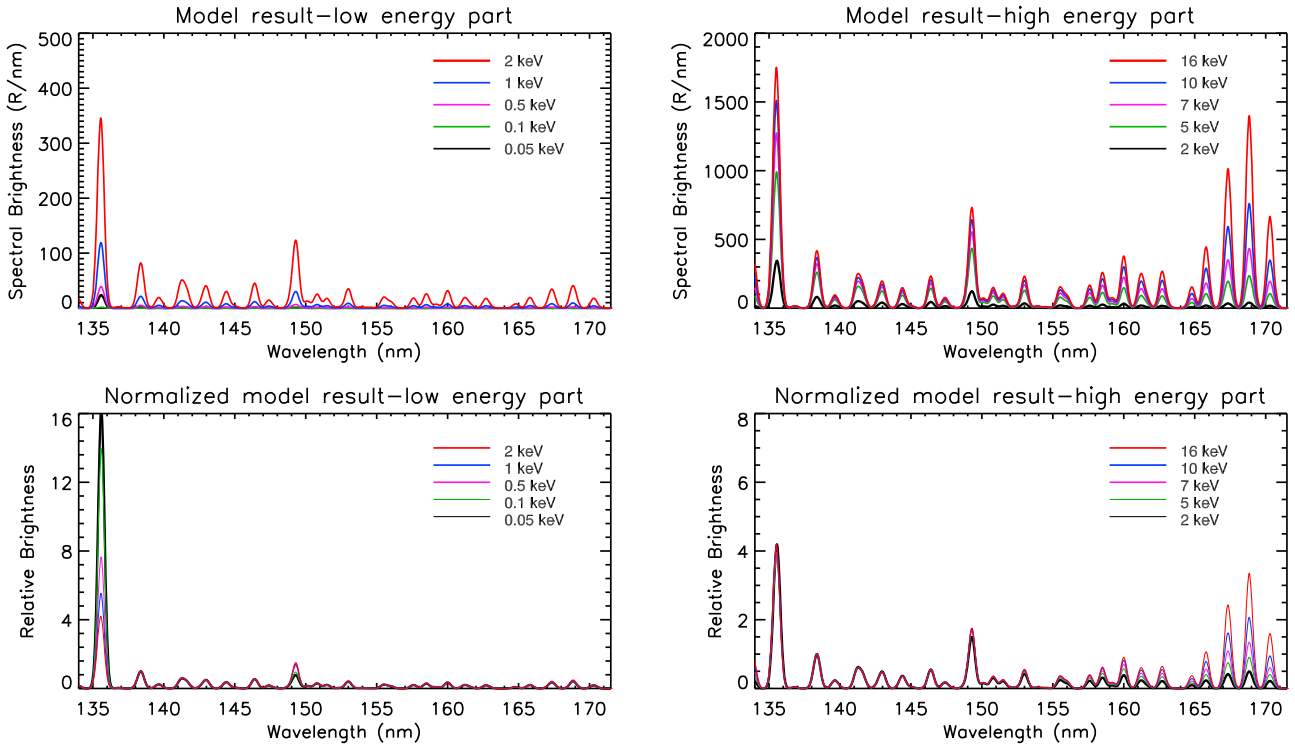

Figure 5. Simulation results of electron energy dependence for FUV auroral emissions from 134.0 nm to 171.5 nm. (top) Low-characteristic energies (0.05 keV–2 keV) and (bottom) high-characteristic energies (2–16 keV). (left) The obtained spectral brightness (rayleigh/nm) and (right) the relative brightness normalized by the intensity at N_2 138.4 nm.

relative intensity of 146.4 nm to 183.8 nm is more or less constant below 2 keV while that of OI 135.6 nm sharply decreases with increasing energy according to Figure 2 of *Germany et al.* [1990]. We have done similar simulations using the model of *Lummerzheim and Lilensten* [1994]. We calculated electron transport with monoenergtic electrons of 0.05, 0.1, 0.5, 1, 2, 5, 7, 10, and 16 keV. Volume emissivity was calculated at grid points, and then radiation transport equation was solved along the line of sight toward the satellite position to obtain intensity with O_2 absorptions taken into account. We fixed the particle number flux as well as all other parameters. As the code does not support the S-band spectral region, we limit our discussions to the L-band spectrum. The results are shown in Figure 5. As Figure 5 (left) shows, the absolute intensity increases over the whole wavelength region as the characteristic energy increases. However, it is clear that the intensity of the OI 135.6 nm line increases faster than those of other lines at low electron energies, while at high energies, the intensities of the long LBH band lines above 160 nm increase faster than those of other lines. The results are more apparent in Figure 5 (right) which display the intensity normalized to the intensity of N_2 138.4 nm, where the O_2 absorption cross section is maximum in the given wavelength range. The relative intensity of OI 135.6 nm line decreases as the electron energy increases from 0.05 to 2 keV, and it virtually saturates above 2 keV. The relative intensities of the long LBH band lines increase with increasing electron energy at high energies. The normalized NI 149.3 nm line seems to increase with increasing electron energy below 0.5 keV but does not change much above 0.5 keV.

[21] It is difficult to apply the simulation results directly to the observations made by STSAT-1 since the observed electron fluxes as well as their spectra change simultaneously. Furthermore, the limited coverage in the energy of ESA makes the comparison more difficult. Electrons below 0.1 keV, whose flux is expected to be large, and therefore expected to have affected the observed OI 135.6 nm line intensity significantly, were not measured. Neither were the electrons above 20 keV. It was demonstrated in our previous study that simulation results agreed better with the observed data when the electron spectrum was extrapolated to 70 keV [*Lee et al.*, 2010]. Nevertheless, the main features obtained in the simulations seem to agree with the observations, especially regarding the behavior of the OI 135.6 nm line and the long LBH band lines. We have plotted the relative intensity of the OI 135.6 nm line to the NI 149.3 nm line in Figure 6a and that of LBHL to LBHS Figure 6b for the five subregions of Figure 1. The characteristic energy is defined by an energy flux divided by a number flux for the given subregion. As can be seen in Figure 6a, the relative intensity of OI 135.6 nm to NI 149.3 nm decreases with increasing energy below 2 keV and is more or less constant above 2 keV, except for region A. The ESA spectrum for region A, the dayside subauroral region, has a shape different from those of other subregions, as shown in Figure 3, with a combination of very soft electrons and high-energy contributions. We believe the discrepancy in the case of region A originates from this peculiar spectral composition of

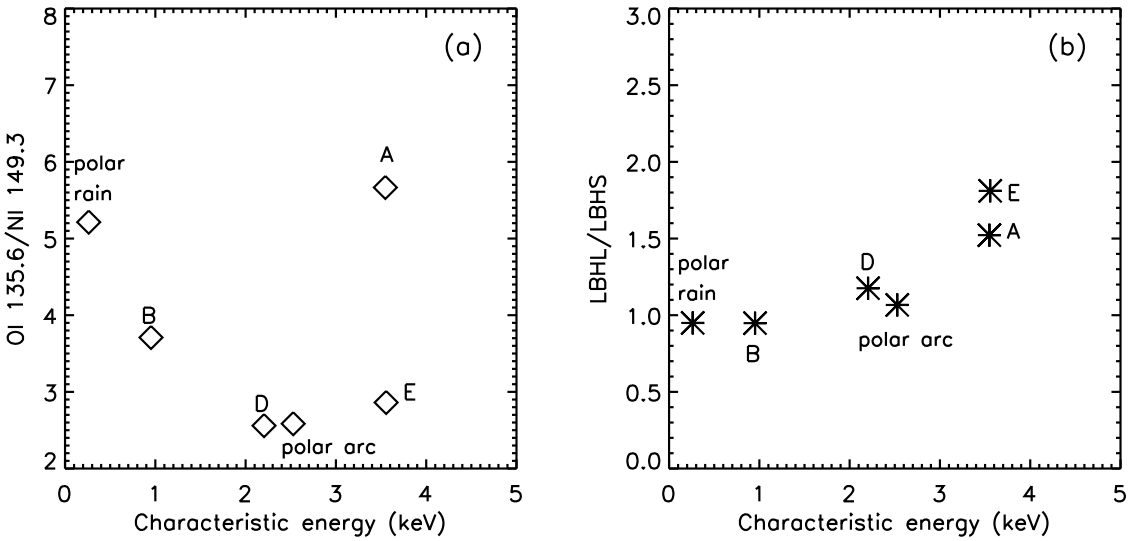

Figure 6. (a) The relative intensity of the OI 135.6 nm line to the NI 149.3 nm line and (b) that of LBHL to LBHS.

electrons: the high characteristic energy comes from the contribution of the bump around 5 keV, while the high relative intensity of OI 135.6 nm to NI 149.3 nm is due to the high flux of soft electrons. The relative intensity of the LBHL band to the LBHS band seems to increase with increasing characteristic energy over the entire energy range up to ~4 keV.

[22] There are three important OI lines observed in this study: OI 98.9 nm, OI 102.6 nm (a mixture of OI 102.7 nm and HI 102.5 nm), and OI 135.6 nm. Their intensity variations in the five subregions can be summarized as follows. In the auroral zone, all of the three OI lines were brighter in the dayside than in the nightside, and it was attributed to the softer ESA spectrum with higher flux at lower energies in the dayside. For the subauroral regions, whose nightside ESA spectrum was harder with higher fluxes over the whole observed energy range than the dayside spectrum, the OI 102.6 nm and OI 135.6 nm lines were brighter in the nightside while the intensity level of the OI 98.9 nm line was still brighter in the dayside. In the polar cap region, for which we compared the polar rain and polar arc spectra, the OI 102.6 nm and OI 135.6 nm lines were brighter in the polar arc where the ESA spectrum was harder, while the intensity levels of the OI 98.9 nm line of the polar rain and the polar arc were more or less similar to each other. The intensity ratio of the OI 135.6 nm line to the OI 98.9 nm line according to the characteristic energies is shown in Figure 7 for the five subregions, and it clearly shows the increasing trend with increasing energy except in the dayside subauroral region whose ESA spectrum consists of soft electrons and high-energy contributions. We believe this dependence of the relative intensity of OI 135.6 nm to OI 98.9 nm originates from the fact that the OI 135.6 nm emission is a spin forbidden transition and much less optically thick than the OI 98.9 nm emission which is a strong resonant transition. Hence, the OI 135.6 nm line observed from the top of the atmosphere responds much better to the energy of precipitating electrons than the OI 98.9 nm line emission.

[23] There have been many efforts to establish a reliable connection of the precipitating energy flux from FUV images, since the images can be taken globally and the information on the precipitation energy is crucial to modeling the polar ionosphere [*Carbary et al.*, 2004]. FIMS data for inverted-V events have also been analyzed in this context by *Lee et al.* [2010]: the result was that the downward electron energy flux correlated well with the LBHL irradiance for the wavelength range 160.0–171.5 nm, but the relationship depended on the spatial scales. The relationship was more or less linear when the spatial scale is large (70 km × 140 km) while the FUV irradiance increased much faster than the energy flux when the spatial scale was small (10 km × 10 km). It was argued that the low-energy contributions are responsible for the slower increase of the FUV irradiance in the case of large spatial scales

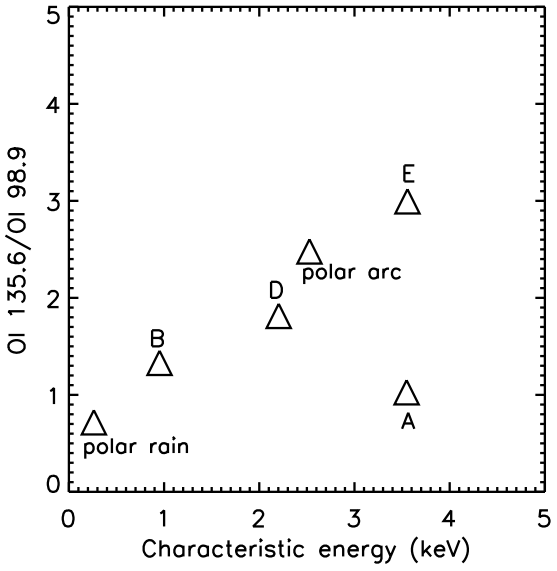

Figure 7. The relative intensity of the OI 135.6 nm line to the OI 98.9 nm line plotted against the characteristic energy for the five subregions.

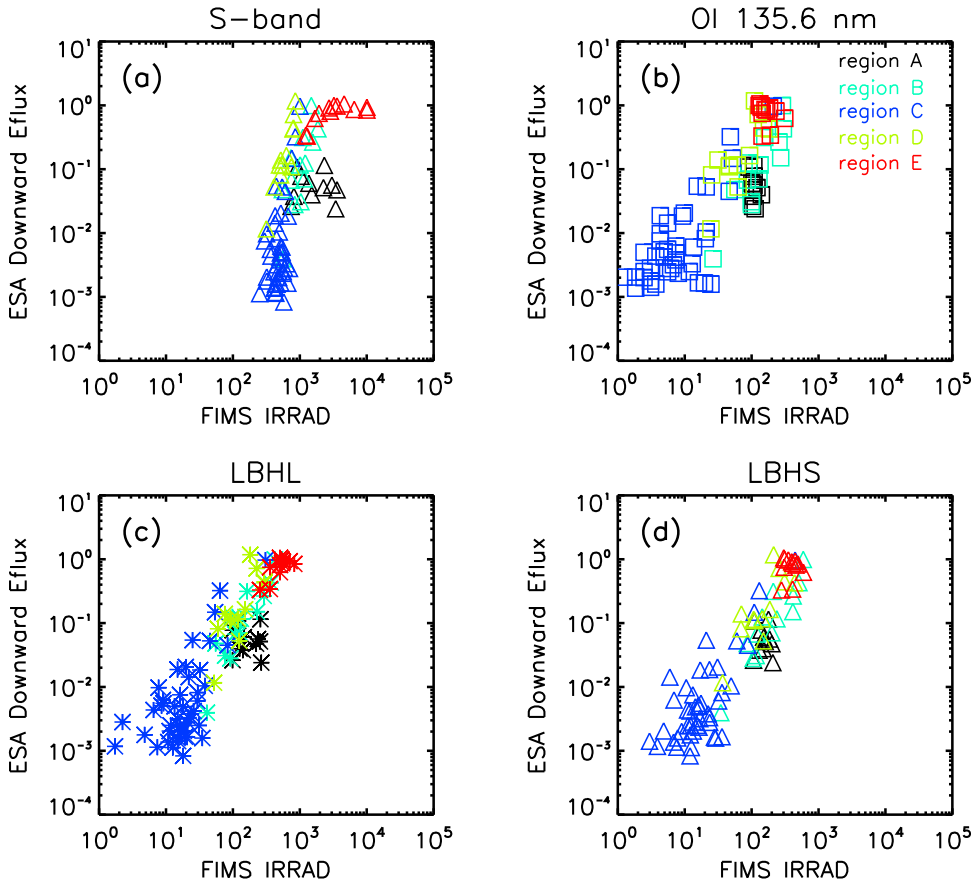

Figure 8. The relationship between the FIMS FUV irradiance (rayleigh) and the downward ESA electron energy flux (ergs/cm^2/s). Each data point is the average of 10 s of observation.

[*Lee et al.*, 2010]. In Figure 8, we have plotted the FUV irradiance against the downward ESA energy flux for the S-band (90.0 nm–115.0 nm), OI 135.6 nm (135.0 nm–136.0 nm), LBHS (140.0 nm–150.0 nm), and LBHL (160.0 nm–171.5 nm). Each data point is an average over a 10 s interval, corresponding to ~75 km on the ground. We can see that the FUV irradiance generally has a good correlation with the downward ESA energy flux, except in the S-band. The rather poor correspondence between the FUV intensity and the ESA energy flux in the S-band plot is probably due to the contributions of the lines of different characteristics mixed in the S-band. For example, the intensity of the ionic NII line in the S-band is enhanced by high-energy particles, while there are no such ionic lines in other bands. Fitting the LBHL data points with a power law $I(x) = Ax^P$, where I is the downward energy flux in ergs/cm^2/s and x is the LBHL irradiance in rayleighs, the spectral index is found to be 1.37, similar to the value 1.28 obtained previously with the large spatial scale averages (~70 km × ~140 km) for inverted-V events [*Lee et al.*, 2010]. With the same power law fitting, the power index p values are 1.13 and 1.57 for OI and LBHS, respectively.

5. Summary

[24] Using the simultaneous observations made by ESA and FIMS on board STSAT-1, we studied the response of the FUV spectrum of the polar region to the changes of precipitating electron characteristics during the period of slightly disturbed geomagnetic conditions.

[25] The FIMS image covered by this observation showed discrete features, embedded in the diffuse continuum background, which are well correlated with monoenergetic electron precipitations in the keV energies. We divided the observed polar region into five subregions: the dayside subauroral region, dayside auroral zone, polar cap, nightside auroral zone, and nightside subauroral region. The present result showed the features consistent with previous observations. For example, the electron spectrum in the dayside subauroral region was dominated by electrons with soft energies of ~100 eV, though high-energy electrons of ~5 keV were also seen with very low fluxes. The discrete arcs observed in the dayside auroral zone were sharper than those observed in the nightside auroral zone, corresponding to the compressed magnetic field structure of the source region of the precipitating electrons, which were also seen to have sharper features compared with those of the nightside auroral zone.

[26] In addition, we obtained some new results regarding the FUV spectral response of these subregions, which had not been previously observed in detail. In the dayside subauroral region, the relative intensity of the OI 135.6 nm line to LBH band lines was higher than in the nightside subauroral region or the auroral zones, which is believed to come from the contributions of soft electrons that were seen in the ESA spectrum of the dayside subauroral region. A

similar effect was also seen in the polar rain where the electron spectrum was very soft. The relative intensity of OI 135.6 nm to the NI 149.3 nm line was calculated for the five subregions and compared with the characteristic energies of these subregions. The result clearly showed the tendency of decrease with increasing characteristic energy for electron energies less than ~2 keV, while it was more or less the same for energies above 2 keV, except in the dayside subauroral region where the ESA spectrum showed a complex structure with a low-energy component mixed with high-energy contributions. On the other hand, the intensities of the LBHL band increased with increasing energy more rapidly than those of the LBHS band, which was attributed to the fact that higher-energy electrons penetrate deeper into the atmosphere and the photons emitted from the lower altitude region suffer stronger O_2 absorption in the LBHS band before they reach the altitude of the satellite.

[27] The observed intensities of the S-band, OI 135.6 nm, LBHS, and LBHL were compared with the precipitating electron energy flux, both averaged over 10 s bins corresponding to ~75 km on the ground. Except in the S-band, which contains lines of different characteristics such as OI 98.9 nm, OI/HI 102.6 nm, NII 108.5 nm, and NI 113.4 nm, the intensities correlated well with precipitating energy flux. When fitted with the power law, $I(x) = Ax^P$, where I is the downward energy flux in ergs/cm^2/s and x is the LBHL irradiance in rayleighs, the spectral index for LBHL was found to be 1.37, similar to the value 1.28 obtained previously with the spatial bins of 70 km × 140 km [*Lee et al.*, 2010].

[28] **Acknowledgments.** FIMS/SPEAR is a joint project of KAIST and KASI (Korea) and UC Berkeley (USA), funded by the Korea MOST and NASA grant NAG5-5355. We acknowledge the use of the OMNI data for the near-Earth solar wind magnetic fields. This research was supported by Basic Science Research Program (2010-0023909) and National Space Laboratory Program through the National Research Foundation of Korea (NRF) funded by the Ministry of Education, Science and Technology.

[29] Robert Lysak thanks the reviewers for their assistance in evaluating this paper.

References

Brittnacher, M., J. Spann, G. Parks, and G. Germany (1997), Auroral observations by the Polar Ultraviolet Imager (UVI), *Adv. Space Res.*, *20*, 1037.

Burch, J. L. (1968), Low-energy electron fluxes at latitudes above the auroral zone, *J. Geophys. Res.*, *73*, 3585.

Carbary, J. F., T. Sotirelis, P. T. Newell, and C.-I. Meng (2004), Correlation of LBH intensities with precipitating particle energies, *Geophys. Res. Lett.*, *31*, L13801, doi:10.1029/2004GL019888.

Chubb, T. A., and G. T. Hicks (1970), Observations of the aurora in the far ultraviolet from OGO 4, *J. Geophys. Res.*, *75*, 1290.

Clark, M. A., and P. H. Metzger (1969), Auroral Lyman-alpha observations, *J. Geophys. Res.*, *74*, 6257.

Edelstein, J., et al. (2006a), The Spectroscopy of Plasma Evolution from Astrophysical Radiation mission, *Astrophys. J.*, *644*, L153.

Edelstein, J., et al. (2006b), The SPEAR instrument and on-orbit performance, *Astrophys. J.*, *644*, L159.

Feldstein, Y. I., and Y. I. Galperin (1985), The auroral luminosity structure in the high-latitude upper atmosphere: Its dynamics and relationship to the large-scale structure of the Earth's Magnetosphere, *Rev. Geophys.*, *23*, 217.

Frank, L. A., and K. L. Ackerson (1971), Observations of charged particle precipitation into the auroral zone, *J. Geophys. Res.*, *76*, 1971.

Frank, L. A., J. D. Craven, J. L. Burch, and J. D. Winningham (1982), Polar views of the Earth's aurora with Dynamics Explorer, *Geophys. Res. Lett.*, *9*, 1001.

Frank, L. A., J. D. Craven, and R. L. Rairden (1985), Images of the Earth's aurora and geocorona from the Dynamics Explorer mission, *Adv. Space Res.*, *5*, 53.

Frank, L. A., et al. (1986), The theta aurora, *J. Geophys. Res.*, *91*, 3177.

Frey, H. U., S. B. Mende, T. J. Immel, J.-C. Gerard, B. Hubert, S. Habraken, J. Spann, G. R. Gladstone, D. V. Bisikalo and V. I. Shematovich (2003), Summary of quantitative interpretation of IMAGE far ultraviolet auroral data, *Space Sci. Rev.*, *109*, 255.

Gerard, J.-C., and C. A. Barth (1976), OGO-4 observations of the ultraviolet auroral spectrum, *Planet. Space Sci.*, *24*, 1059.

Germany, G. A., M. R. Torr, P. G. Richards, and D. G. Torr (1990), The dependence of modeled OI 1356 and N_2 Lyman Birge Hopfield auroral emissions on the neutral atmosphere, *J. Geophys. Res.*, *95*, 7725.

Germany, G. A., M. R. Torr, D. G. Torr, and P. G. Richards (1994), Use of FUV auroral emissions as diagnostic indicators, *J. Geophys. Res.*, *99*, 383.

Gussenhoven, M. S. (1982), Extremely high latitude auroras, *J. Geophys. Res.*, *87*, 2401.

Hardy, D. A., M. S. Gussenhoven, and E. Holeman (1985), A statistical model of auroral electron precipitation, *J. Geophys. Res.*, *90*, 4229.

Huffman, R. E., F. J. LeBlanc, J. C. Larrabee, and D. E. Paulsen (1980), Satellite vacuum ultraviolet airglow and auroral observations, *J. Geophys. Res.*, *85*, 2201.

Ishimoto, M., C.-I. Meng, G. J. Romick, and R. E. Huffman (1988), Auroral electron energy and flux from molecular nitrogen ultraviolet emissions observed by the S3-4 satellite, *J. Geophys. Res.*, *93*, 9854.

Joki, E. G., and J. E. Evans (1969), Satellite measurements of auroral ultraviolet and 3914-A radiation, *J. Geophys. Res.*, *74*, 4677

Kunitake, M., and T. Oguti (1984), Spatial-temporal characteristics of flickering spots in flickering auroras, *J. Geomagn. Geoelectr.*, *36*, 121.

Lee, C. N., et al. (2010), Spectral observations of FUV auroral arcs and comparison with inverted-V precipitating electrons, *J. Geophys. Res.*, *115*, A09223, doi:10.1029/2009JA015071.

Lee, J.-J., et al. (2005), Energy spectra of ~170–360 keV electron microbursts measured by the Korean STSAT-1, *Geophys. Res. Lett.*, *32*, L13106, doi:10.1029/2005GL022996.

Lummerzheim, D., and J. Lilensten (1994), Electron transport and energy degradation in the ionosphere: Evaluation of the numerical solution, comparison with laboratory experiments and auroral observations, *Ann. Geophys.*, *12*, 1039.

Makita, K., C.-I. Meng, and S.-I. Akasofu (1991), Transpolar auroras, their particle precipitation, and IMF B_y component, *J. Geophys. Res.*, *96*, 14,085.

McFadden, J. P., C. W. Carlson, M. H. Boehm, and T. J. Hallinan (1987), Field-aligned electron flux oscillations that produce flickering aurora, *J. Geophys. Res.*, *92*, 11,133.

Newell, P. T., and C.-I. Meng (1992), Mapping the dayside ionosphere to the magnetosphere according to particle precipitation characteristics, *Geophys. Res. Lett.*, *19*, 609.

Newell, P. T., and C.-I. Meng (1995), Creation of theta-auroras: The isolation of plasma sheet fragments in the polar cap, *Science*, *270*, 1338.

Newell, P. T., Y. I. Feldstein, Y. I. Galperin, and C.-I. Meng (1996), Morphology of nightside precipitation, *J. Geophys. Res.*, *101*, 10,737.

Newell, P. T., A. R. Lee, K. Liou, S. Wing, and M. Hairston (2010), Multisatellite low-altitude observations of a magnetopause merging burst, *J. Geophys. Res.*, *115*, A11204, doi:10.1029/2010JA015438.

Paresce, F., S. Chakrabarti, S. Bowyer, and R. Kimble (1983a), The extreme ultraviolet spectrum of dayside and nightside aurorae: 800–1400 Å, *J. Geophys. Res.*, *88*, 4905.

Paresce, F., S. Chakrabarti, R. Kimble, and S. Bowyer (1983b), The 300- to 900-Å of a nightside aurora, *J. Geophys. Res.*, *88*, 10,247.

Park, H., P. D. Feldman, and W. G. Fastie (1977), The extreme ultraviolet (750–1230 Å) spectrum of an aurora, *Geophys. Res. Lett.*, *4*, 41.

Paxton, L. J., et al. (1999), Global ultraviolet imager (GUVI): Measuring composition and energy inputs for the NASA Thermosphere Ionosphere Mesosphere Energetics and Dynamics (TIMED) mission, *Proc. SPIE*, *3756*, 265–276.

Sandholt, P. E., H. C. Carlson, and A. Egeland (2002), *Dayside and Polar Cap Aurora*, *Astrophys. Space Sci. Library*, vol. 270, Kluwer Acad., Dordrecht, Netherlands.

Sandholt, P. E., M. Dyrland, and C. J. Farrugia (2006), Dayside aurorae and polar arcs under south-east IMF orientation, *Ann. Geophys.*, *24*, 3421.

Strickland, D. J., J. R. Jasperse, and J. A. Whalen (1983), Dependence of auroral FUV emissions on the incident electron spectrum and neutral atmosphere, *J. Geophys. Res.*, *88*, 8051.

Torr, M. R., et al. (1995), A far ultraviolet imager for the international solar-terrestrial physics mission, *Space Sci. Rev.*, *71*, 329.

Victor, G. A., P. McKenna, and A. Dalgarno (1976), Auroral emission at 1084Å, *Planet. Space Sci.*, *24*, 405.

Winningham, J. D., and W. J. Heikkila (1974), Polar cap auroral electron fluxes observed with Isis 1, *J. Geophys. Res.*, *79*, 949.

J. Edelstein, Space Sciences Laboratory, University of California, 7 Gauss Way, Berkeley, CA 94720, USA.

W. Han, J. A. Hwang, C. N. Lee, and J.-J. Lee, Korea Astronomy and Space Science Institute, Daejeon, 305-348, South Korea. (cnlee@kasi.re.kr)

K. W. Min, Department of Physics, Korea Advanced Institute of Science and Technology, Daejeon, 305-701, South Korea. (kwmin@kaist.ac.kr)

J. Park, Helmholtz Centre Potsdam, GFZ Potsdam, Sect. 2.3, Telegrafenberg, D-14473 Potsdam, Germany.